Nanoscale Advances

ROYAL SOCIETY OF CHEMISTRY

COMMUNICATION

View Article Online
View Journal | View Issue

Cite this: *Nanoscale Adv.*, 2026, **8**, 2215

Received 26th December 2025
Accepted 24th February 2026

DOI: 10.1039/d5na01166c

rsc.li/nanoscale-advances

A pH-stable dynamic DNA nanomachine with controllable conformational switching

Lixuan Lin,[ab] Kaiyi Liang,[c] Xiuli Gao,[d] Jiang Li,[e] Linjie Guo, *[e] Kai Jiao *[e] and Lihua Wang[ef]

The heterogeneity of physiological pH poses a major challenge to the stability and function of dynamic DNA nanomachines. Here, we systematically evaluate the performance of a six-helix DNA nanomachine (6H-NNM) as a model system. It maintains reversible, strand-displacement-driven conformational switching across pH 5–9 (>81% intact after 8 h) and remains functional under lysosome-mimicking acidic conditions. Our study provides an evaluation framework and performance benchmark for dynamic DNA devices in complex biological settings.

Nucleic acid nanostructures, owing to their programmability, molecular precision, and biocompatibility, have been extensively applied in molecular diagnostics, drug delivery, and targeted therapeutic applications.[1–5] The emergence of dynamic nucleic acid nanotechnology, particularly designs based on strand displacement reactions (SDR) and ligand-induced conformational transitions, has enabled static DNA architectures to evolve into responsive nanomachines capable of signal sensing, logic processing, and controlled actuation.[6–8] Among these, SDR-based nanomachines offer modularity and predictable kinetics, supporting applications such as molecular computation, stimulus-responsive regulation, and precision drug delivery.[9–12]

pH-driven nanomachines incorporating i-motifs or triplex DNA have demonstrated DNA's ability to function under specific pH conditions by transducing pH changes into mechanical motion.[13,14] However, these devices are inherently designed to respond to pH itself, often within narrow ranges. Despite these advances, the practical deployment of SDR-based nanomachines in biological environments remains challenging. Physiological systems exhibit pronounced pH heterogeneity across tissues and intracellular compartments, which critically affects nucleic acid stability and dynamic behavior.[15–17] For example, lysosomes are strongly acidic (pH 4.5–5.5), the cytosol is near neutral (pH ≈ 7.2), and mitochondria are mildly alkaline (pH ≈ 8.0).[18] Tissue-level variations are also significant, from acidic tumor microenvironments to the gastric lumen.[19] Such pH fluctuations can induce depurination, disrupt hydrogen bonding, and weaken base-pairing, impairing the structural integrity and conformational switching.[20–22] For SDR-based nanomachines, a systematic quantification of their structural stability and switching efficiency across this physiologically critical pH spectrum remains lacking.

To address this, we constructed a dynamic DNA nanomachine (6H-NNM) based on the well-characterized six-helix bundle (6HB), chosen for its intrinsic structural rigidity.[23] We integrated a strand-displacement-driven reversible molecular lock to enable programmable conformational switching in response to nucleic acid inputs. We then systematically evaluated its structural stability and switching kinetics across tested range pH 5–11. Our results demonstrate that 6H-NNM remains structurally intact and exhibits controllable switching dynamics within the physiologically critical pH window of 5–9, with reliable conformational switching even under lysosome-mimicking conditions (pH 4.5). This systematic evaluation provides a quantitative performance benchmark and highlights the importance of mechanically coherent scaffolds for engineering pH-resilient DNA nanodevices.

The 6H-NNM was assembled from a reported 6HB (~22 nm long, ~7.5 nm diameter).[11,24] It comprises two semi-tubular three-helix subunits connected by two DNA locks at the subunit edges. These locks enable toehold-mediated strand displacement, allowing reversible conformational switching upon addition of external DNA triggers (Unlock and Relock

[a]CAS Key Laboratory of Interfacial Physics and Technology, Shanghai Institute of Applied Physics, Chinese Academy of Sciences, Shanghai, 201800, China
[b]University of Chinese Academy of Sciences, Beijing, 100049, China
[c]Radiology Department of Jiading District Central Hospital Affiliated Shanghai University of Medicine &Health Sciences, Shanghai, 201800, China
[d]State Key Laboratory of Transducer Technology, Shanghai Institute of Microsystem and Information Technology, Chinese Academy of Sciences, Shanghai, 200050, China
[e]Institute of Materiobiology, College of Sciences, Shanghai University, Shanghai, 200444, China. E-mail: guolinjie@shu.edu.cn; kjiao@shu.edu.cn
[f]Shanghai Collaborative Innovation Center of Intelligent Sensing Chip Technology, Shanghai University, Shanghai, 200444, China

keys) (Fig. 1a, sequences listed in Table S1). For real-time monitoring, a fluorescence reporter (Alexa Fluor 488 and BHQ1) was incorporated into one lock. In the closed state, fluorescence was quenched due to the short fluorophore–quencher distance; unlocking separated the pair and restored fluorescence.

6H-NNM was assembled by thermal annealing of component strands in synthesis buffer (pH 8) from 90 °C to room temperature, yielding the initial closed conformation. At room temperature, addition of the Unlock key converted 6H-NNM to the open state, while subsequent addition of the Relock key restored the closed state (Fig. 1a; sequences in Table S2). Polyacrylamide gel electrophoresis (PAGE) revealed single, well-defined migration bands for both conformations, indicating high structural integrity and homogeneity (Fig. S1). AFM images and height profiles further confirmed the conformational transition (Fig. 1b): closed 6H-NNM appeared as compact, nearly monodisperse rod-like particles with a height of ~4 nm, whereas Unlock key treatment produced an open structure with a reduced height of ~2 nm, while maintaining connectivity between the two three-helix subunits. These results demonstrate that external nucleic acid inputs induce a defined conformational change.

Real-time fluorescence kinetics measured at pH 8 further verified the dynamic switching behavior (Fig. 1c). Upon addition of the Unlock key, fluorescence intensity increased and reached a steady-state plateau within ~5 min, while no change was observed in the absence of the key. Subsequent addition of the Relock key led to a decrease in fluorescence to a new plateau, confirming reversible switching between the closed and open states. Together, these results establish that 6H-NNM exhibits high structural fidelity and well-regulated reversible conformational switching.

We next evaluated the structural stability of 6H-NNM under different pH conditions by incubating preassembled structures in buffers ranging from pH 5 to 11 for up to 8 h at room temperature. PAGE analysis showed that 6H-NNM maintained single, sharp bands across pH 5–9 at all time points, indicating substantial structural integrity under acidic to mildly basic conditions (Fig. 2a and S2). In contrast, at pH 10 and 11, electrophoretic bands became smeared or disappeared, suggesting rapid degradation under strongly alkaline conditions. Densitometric analysis revealed that 6H-NNM exhibited maximal stability at pH 8, retaining a band ratio of 0.70 after 8 h. At pH 5 and 6, the band ratios gradually decreased from 0.70 to 0.57 and from 0.76 to 0.65, corresponding to degradation levels of approximately 18.1% and 14.5%, respectively. In contrast, under strongly alkaline conditions (pH ≥ 10), the initial band ratios were already as low as 0.18 and 0.10 at 0 h, confirming rapid destabilization (Fig. 2b and S3). These results indicate that 6H-NNM maintains substantial structural stability within the functional range of pH 5–9. The observed stability in this range likely benefits from the structural reinforcement of the multi-helix architecture and the Mg^{2+} in the buffer system. In contrast, degradation at high pH likely arises from base deprotonation-induced strand dissociation and reduced Mg^{2+}-mediated structural support.

We then assessed the reversible switching behavior of 6H-NNM across the tested range of pH 5–11. A fourfold excess of the Unlock key followed by a sixteen-fold excess of the Relock key was sequentially added to preassembled 6H-NNM solutions adjusted to pH 5–11, and the real-time fluorescence response was monitored. Within pH 5–9, 6H-NNM exhibited clear and reproducible reversible switching (Fig. 3a). Addition of the Unlock key induced a rapid increase in fluorescence, reaching a plateau within ~5 min, consistent with the formation of the open state through spatial separation of the fluorophore–quencher pair. Subsequent addition of the Relock key restored fluorescence quenching within a similar timescale, confirming efficient reclosure. In contrast, at pH 10 and 11, fluorescence increased continuously upon sequential key addition and showed pronounced fluctuations, indicating structural destabilization and loss of controlled switching, consistent with the pH-dependent stability analysis.

Quantitative kinetic analysis of the fluorescence traces within pH 5–9 revealed pronounced pH-dependent effects. Kinetic fitting yielded the steady-state fluorescence intensity (F_{inf}), area under the curve (AUC), apparent rate constant (k_{obs}), half-time (t_{half}), and recovery ratio. The fastest and most

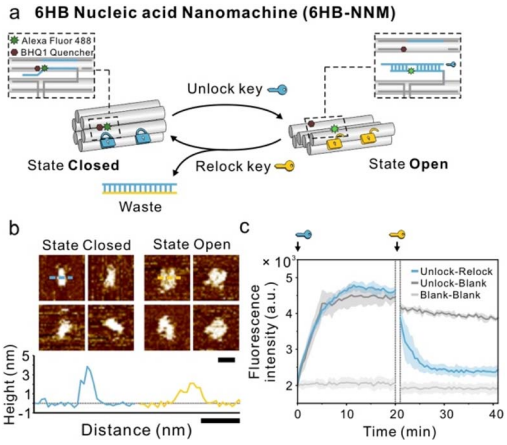

Fig. 1 Design and reversible switching of the 6H-NNM. (a) Schematic of 6H-NNM with strand-displacement–driven reversible switching. (b) Atomic force microscopy (AFM) images of the closed and open states with representative height profiles, scale bar, 20 nm. (c) Fluorescence kinetics showing reversible switching; data are mean ± s.d. (n = 3 technical replicates).

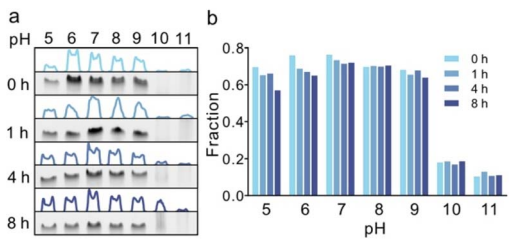

Fig. 2 Stability analysis of 6H-NNM under tested pH conditions. (a) PAGE analysis after incubation across a tested pH range of 5–11 for 0–8 h at room temperature, with densitometric quantification. (b) Fraction of intact 6H-NNM as a function of time under different pH conditions.

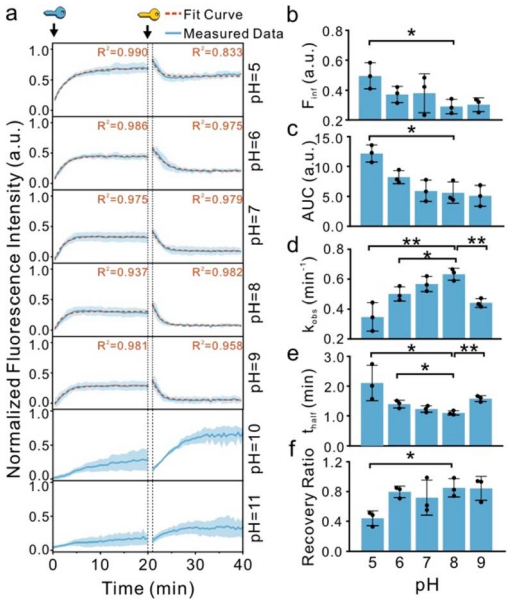

Fig. 3 Reversible switching kinetics of 6H-NNM across different pH conditions. (a) Fluorescence trajectories and fit curve at pH 5–11 upon sequential addition of Unlock and Relock keys. (b–f) Quantitative kinetic parameters extracted from (a), including steady-state fluorescence (F_{inf}), apparent rate constant (k_{obs}), half-time (t_{half}), area under the curve (AUC), and recovery ratio. (mean ± s.d., n = 3 technical replicates). Statistical comparisons were performed using one-way ANOVA; *p < 0.05, **p < 0.01.

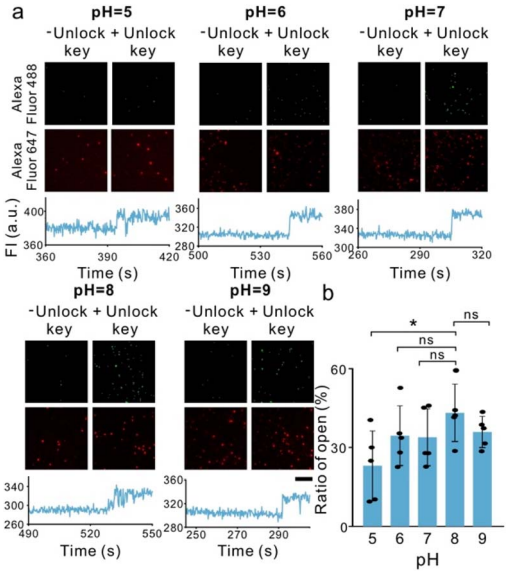

Fig. 4 Single-molecule analysis of 6H-NNM conformational switching. (a) TIRF imaging of individual 6H-NNM switching events at pH 5–9 with representative fluorescence trajectories. Scale bar, 5 μm. (b) Switching efficiency quantified as the fraction of nanomachines in the open state after Unlock key addition (mean ± s.d., n = 5 technical replicates). Statistical analysis was performed using one-way ANOVA; * indicates p < 0.05. FI (a.u.) denotes Fluorescence Intensity (a.u.).

efficient switching was observed at pH 8, with the highest k_{obs} (0.63 min^{-1}), shortest t_{half} (1.10 min), and maximum recovery ratio (85.0%). Significant deviations occurred under acidic conditions. At pH 5, while F_{inf} and AUC increased by ~1.7 and ~2.2-fold relative to pH 8 (Fig. 3b, c), but this was accompanied by a substantially reduced switching rate (k_{obs} = 0.35 min^{-1}, Fig. 3d, e) and a significantly lower recovery ratio (44.1%, Fig. 3f). This combination of increased opening amplitude, slower kinetics, and diminished reversibility suggests partial destabilization of the closed state under acidic stress, rather than improvement in functional performance.[25–27] Overall, pH 7–8 is the optimal window for speed and reversibility, while controllable switching is maintained across the functional range of pH 5–9.

Single-molecule conformational switching was directly visualized using total internal reflection fluorescence (TIRF) microscopy. 6H-NNM was labeled with Alexa Fluor 647 to quantify nanomachine number, while switching events were detected *via* fluorescence changes in the Alexa Fluor 488 channel following Unlock key addition. Across pH 5–9, Unlock key addition resulted in a marked increase in Alexa Fluor 488 fluorescence spots. Representative fluorescence trajectories exhibited stepwise intensity increases characteristic of individual switching events (Fig. 4a and S4). Analysis at 0.2 s/frame resolution showed predominantly single-step transitions, consistent with a concerted switching mechanism facilitated by the kinetic equivalence of the two identical locks. Quantitative analysis revealed that the highest fraction of open-state events occurred at pH 8 (43.2%), exceeding those observed under other pH conditions (23.0–35.9%) (Fig. 4b). This trend is consistent with the ensemble kinetics and reflects the faster switching dynamics at pH 8 within the finite temporal resolution of single-molecule measurements. These results confirm that 6H-NNM maintains controllable conformational switching at the single-molecule level across physiologically relevant pH conditions.

Finally, we tested 6H-NNM under physiologically relevant acidic conditions using artificial lysosomal fluid (ALF, pH 4.5, Table S3), a widely used model that recapitulates key physicochemical features of the lysosomal microenvironment, including acidity, ionic strength, and salt composition.[28] In ALF, sequential addition of Unlock and Relock keys induced clear fluorescence increases and decreases, respectively, demonstrating reversible opening and closing (Fig. 5a). Notably, the fluorescence signal after unlocking did not reach a stable plateau but decayed over time. Extended incubation experiments revealed that this decay profile closely matched that of a free fluorophore-labeled ssDNA (Fig. S5), indicating the signal loss primarily reflects fluorophore photophysics in ALF rather than structural degradation of 6H-NNM. Comparison with fitted kinetic curves obtained at pH 5 and pH 8 revealed that the initial switching behavior in ALF closely resembled that under acidic conditions, while the later-stage fluorescence gradually decreased to levels comparable to pH 8 (Fig. 5b). Kinetic fitting of the initial reaction phase (R^2 > 0.9) showed that the apparent switching rate in ALF was relatively high compared to pH 5 and pH 8 (Fig. 5c), The elevated rate in ALF likely results from a combination of acid-enhanced strand invasion and the strong electrostatic screening provided by the high ionic strength of ALF, which together may override the base-pairing destabilization typically observed at low pH. These results show that 6H-

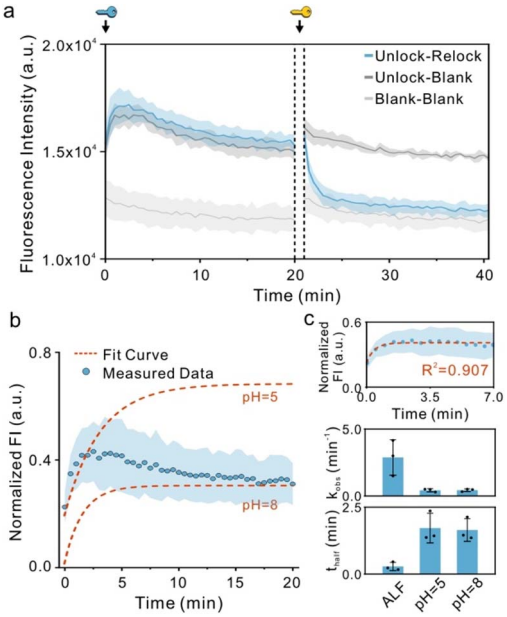

Fig. 5 Reversible switching of 6H-NNM in ALF. (a) Fluorescence trajectories upon sequential addition of Unlock and Relock keys in ALF. (b) Comparison of opening kinetics in ALF with fitted curves obtained at pH 5 and pH 8. (c) Apparent switching rates extracted from the initial reaction phase (R^2 > 0.9) and compared with pH 5 and pH 8 (mean ± s.d., n = 3 technical replicates). Normalized FI (a.u.) denotes Normalized Fluorescence Intensity (a.u.).

NNM retains conformational responsiveness in lysosome-mimicking environments. However, the non-ideal fluorescence traces highlight that its behavior is less controlled in ALF than in standard buffers, underscoring the challenges posed by complex physiological conditions.

In summary, we have established a six-helix DNA nanomachine (6H-NNM) as a model system for evaluating pH resilience. It maintains structural integrity and controllable conformational switching across the physiologically relevant pH window of 5–9, and remains responsive in lysosome-mimicking fluid. This study provides a crucial performance benchmark and demonstrates that structurally coherent multi-helix scaffolds can sustain dynamic function under pH stress. While the operational capability in complex ALF is confirmed, signal variations indicate the need for further engineering toward reliable intracellular use. Future efforts extending this framework, such as probing switching intermediates and mechanisms, assessing multi-cycle endurance and comparing diverse architectural motifs, will further advance the design of environmentally robust DNA nanodevices.

Conflicts of interest

There are no conflicts to declare.

Data availability

All data supporting this article have been included in the main text or the supplementary information (SI). Supplementary information: materials, DNA sequences, methods, gel electrophoresis and densitometric quantification, single-molecular fluorescence images.

Acknowledgements

This work was supported by the National Key Research and Development Program (2023YFB3208200), and the National Natural Science Foundation of China (22325406, 32301185, 22393931, and 22204100).

Notes and references

1 C. Wiraja, Y. Zhu, D. C. S. Lio, D. C. Yeo, M. Xie, W. Fang, Q. Li, M. Zheng, M. Van Steensel, L. Wang, C. Fan and C. Xu, *Nat. Commun.*, 2019, **10**, 1147.
2 D. W. Jiang, Z. L. Ge, H. J. Im, C. G. England, D. L. Ni, J. J. Hou, L. H. Zhang, C. J. Kutyreff, Y. J. Yan, Y. Liu, S. Y. Cho, J. W. Engle, J. Y. Shi, P. Huang, C. H. Fan, H. Yan and W. B. Cai, *Nat. Biomed. Eng.*, 2018, **2**, 865–877.
3 F. F. Yin, H. P. Zhao, S. S. Lu, J. W. Shen, M. Li, X. H. Mao, F. Li, J. Y. Shi, J. Li, B. J. Dong, W. Xue, X. L. Zuo, X. R. Yang and C. H. Fan, *Nat. Nanotechnol.*, 2023, **18**, 677–686.
4 S. Dey, C. Fan, K. V. Gothelf, J. Li, C. Lin, L. Liu, N. Liu, M. A. D. Nijenhuis, B. Saccà, F. C. Simmel, H. Yan and P. Zhan, *Nat. Rev. Methods Primers*, 2021, **1**, 13.
5 T. Zhang, T. R. Tian, R. H. Zhou, S. H. Li, W. J. Ma, Y. X. Zhang, N. X. Liu, S. R. Shi, Q. S. Li, X. P. Xie, Y. C. Ge, M. T. Liu, Q. Zhang, S. Y. Lin, X. X. Cai and Y. F. Lin, *Nat. Protoc.*, 2020, **15**, 2728–2757.
6 D. Y. Zhang and G. Seelig, *Nat. Chem.*, 2011, **3**, 103–113.
7 S. M. Douglas, I. Bachelet and G. M. Church, *Science*, 2012, **335**, 831–834.
8 S. P. Li, Q. Jiang, S. L. Liu, Y. L. Zhang, Y. H. Tian, C. Song, J. Wang, Y. G. Zou, G. J. Anderson, J. Y. Han, Y. Chang, Y. Liu, C. Zhang, L. Chen, G. B. Zhou, G. J. Nie, H. Yan, B. Q. Ding and Y. L. Zhao, *Nat. Biotechnol.*, 2018, **36**, 258–264.
9 G. Chatterjee, N. Dalchau, R. A. Muscat, A. Phillips and G. Seelig, *Nat. Nanotechnol.*, 2017, **12**, 920–927.
10 J. Wang, S. Liu, X. Liu, Y. Chen, J. Liu, K. Wang, K. Quan and J. Huang, *ACS Nano*, 2025, **19**, 39420–39429.
11 Y. Zhao, S. T. Cao, Y. Wang, F. Li, L. X. Lin, L. J. Guo, F. Wang, J. Chao, X. L. Zuo, Y. Zhu, L. H. Wang, J. Li and C. H. Fan, *Nat. Mach. Intell.*, 2023, **5**, 980–990.
12 J. Yin, S. Y. Wang, J. H. Wang, Y. W. Zhang, C. H. Fan, J. Chao, Y. Gao and L. H. Wang, *Nat. Mater.*, 2024, **23**, 854–862.
13 S. S. Lu, J. L. Shen, C. H. Fan, Q. Li and X. R. Yang, *Adv. Sci.*, 2021, **8**, 2100328.
14 L. Song, Y. Zhuge, X. L. Zuo, M. Li and F. Wang, *Adv. Sci.*, 2022, **9**, e2200327.
15 A. Keller and V. Linko, *Angew. Chem., Int. Ed. Engl.*, 2020, **59**, 15818–15833.
16 J. Won, S. Cho, K. R. Kim, S. Kim and D. R. Ahn, *Adv. Drug Delivery Rev.*, 2025, **225**, 115682.
17 A. R. Chandrasekaran, *Nat. Rev. Chem.*, 2021, **5**, 225–239.

18 N. Demaurex, *News Physiol. Sci.*, 2002, **17**, 1–5.
19 N. Procházková, M. F. Laursen, G. La Barbera, E. Tsekitsidi, M. S. Jorgensen, M. A. Rasmussen, J. Raes, T. R. Licht, L. O. Dragsted and H. M. Roager, *Nat. Microbiol.*, 2024, **9**, 3210–3225.
20 T. Lindahl, *Nature*, 1993, **362**, 709–715.
21 G. M. Segers-Nolten, N. M. Sijtsema and C. Otto, *Biochemistry*, 1997, **36**, 13241–13247.
22 G. J. Puppels, C. Otto, J. Greve, M. Robert-Nicoud, D. J. Arndt-Jovin and T. M. Jovin, *Biochemistry*, 1994, **33**, 3386–3395.
23 H. Joshi, A. Dwaraknath and P. K. Maiti, *Phys. Chem. Chem. Phys.*, 2015, **17**, 1424–1434.
24 A. Kuzuya, R. Wang, R. Sha and N. C. Seeman, *Nano Lett.*, 2007, **7**, 1757–1763.
25 L. Wang, C. C. Gong, X. Z. Yuan and G. Wei, *Nanomaterials*, 2019, **9**, 285.
26 X. Wang, H. Zhang, P. P. He, X. Du, Y. Shen, W. Cai and W. Guo, *Small*, 2025, **21**, e2404549.
27 N. G. Economos, S. Oyaghire, E. Quijano, A. S. Ricciardi, W. M. Saltzman and P. M. Glazer, *Molecules*, 2020, **25**, 735.
28 A. MilosevicAc, J. Bourquin, D. Burnand, P. Lemal, F. Crippa, C. A. Monnier, L. Rodriguez-Lorenzo, A. Petri-Fink and B. Rothen-Rutishauser, *Chimia (Aarau)*, 2019, **73**, 55–58.